

# A novel neutron texture diffractometer analyzing method with Convolutional Neural Networks for Face-Centered Cubic Material\*

Bokai Zhao,<sup>1,2</sup> Weimin Gan,<sup>3</sup> Danmin Liu,<sup>4</sup> Xiaolong Liu,<sup>1,2</sup> Yuhua Hou,<sup>1,2</sup> Yuqing Li,<sup>1,2</sup> Tianfu Li,<sup>1,2</sup> Kai Sun,<sup>1</sup> Xueshen Jiao,<sup>1</sup> Meijuan Li,<sup>1,2,†</sup> Dongfeng Chen,<sup>1,2,‡</sup> and Yingxun Zhang<sup>1,§</sup>

<sup>1</sup>Department of Nuclear Physics, China Institute of Atomic Energy, Beijing 102413, China

<sup>2</sup>Key Laboratory of Neutron Scattering Technology and Application,

China National Nuclear Corporation, Beijing 100822, China

<sup>3</sup>GEMS at MLZ, Helmholtz-Zentrum Hereon D-85748, Garching, Germany

<sup>4</sup>College of Materials Science and Engineering, Beijing University of Technology, Beijing 100124, China

In this study, we propose a convolutional neural network (CNN) model aimed at inferring texture types and their volume fractions from neutron diffractometer data. The model is trained using labeled texture data of face-centered cubic (FCC) materials, sourced from X-ray diffraction (XRD) measurements. The effectiveness of the model is evaluated using data obtained from neutron diffraction. Compared to traditional data analysis methods, the CNN model not only offers fast and accurate predictions of texture components and their volume fractions, but also demonstrates strong generalization ability. Even under a certain signal-to-noise ratio, the CNN model maintains high accuracy in inferring texture types and their volume fractions. This capability could facilitate the operation of neutron texture diffractometers at lower neutron beam intensities in the future, thus improving both the efficiency of texture analysis.

Keywords: convolutional neural networks, texture, neutron diffraction, X-ray diffraction, face-centered cubic material

## I. INTRODUCTION

The crystallographic texture, defined as the preferred orientation distribution of grains in polycrystalline materials, induces anisotropy in material properties[1–3] and consequently affects both processing behavior and service performance. Moreover, texture serves as a critical diagnostic parameter in material failure analysis[4]. Therefore, precise texture characterization is fundamental for optimizing texture control strategies, refining processing parameters, and enhancing material performance. Current texture characterization methodologies employ multiple experimental techniques, including electron backscatter diffraction (EBSD)[5], X-ray diffraction (XRD)[6], synchrotron X-ray diffraction[7], and neutron diffraction (NuD)[8], which provide complementary characterization capabilities for polycrystalline systems.

Quantitative analysis of texture distributions requires diffraction pattern acquisition across multiple crystallographic orientations and the utility of a neutron detector. Currently, a two-dimensional position sensitive detector is usually used for improving the measurement efficiency of neutron texture diffractometer[9], and more data needs to be collected in a short period. Consequently, two main challenges arise in texture data processing. First, collecting a large amount of data slows down the processing speed and

impedes real-time assessment of the texture information of the measured materials. This is because the texture data processing involves multiple steps, including data acquisition, pre-processing to get the pole figure, orientation distribution function (ODF), and texture component analysis[10]. Second, the accuracy of the current texture analysis methods is often compromised by significant errors in diffraction peak intensity fitting, particularly for polycrystalline materials that exhibit weak overall texture, a combination of strong and weak texture components, or strongly overlapping diffraction peaks. It naturally requires seeking a powerful data analysis method.

State-of-the-art machine learning (ML) technology has demonstrated remarkable capabilities in materials characterization, as evidenced by successful applications in various experimental techniques, including XRD[11–15], EBSD[16–18], and synchrotron X-ray diffraction[19–21]. These achievements have motivated researchers at the neutron scattering laboratory to explore the ML potential in related domains. Recent studies have documented ML implementations in neutron instrumentation, specifically single-crystal diffractometers[22], neutron reflectometers[23, 24], and imaging facilities[25]. Nevertheless, ML deployment in neutron texture diffractometers remains uninvestigated.

\* Supported by the National Natural Science Foundation of China (Grant 12275359), China National Nuclear Corporation (Grant FY222506000101), National Natural Science Foundation of China (Grant 12075321), Continuous Basic Scientific Research Project (16BJ010261224864) and Director's Foundation of China Institute of Atomic Energy (16YZ010270324221). The authors thank Prof. Chun-Wang Ma's helpful suggestions.

† Corresponding author, mjli@ciae.ac.cn

‡ Corresponding author, dongfeng@ciae.ac.cn

§ Corresponding author, zhyx@ciae.ac.cn

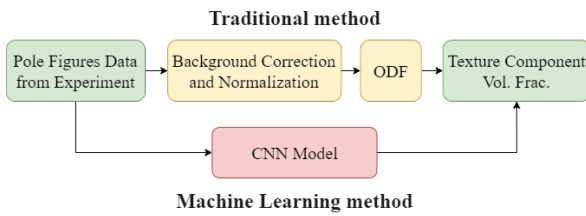
In this work, we propose a machine learning-based framework for texture analysis in crystalline materials. The paper is organized as follows. First, a face-centered cubic (FCC) material texture dataset, derived from high-resolution XRD measurements, is established. Subsequently, a customized convolutional neural network (CNN) architecture is developed and optimized using this dataset. Finally, the model is validated for accuracy and noise immunity.

57

## II. METHODS

### 58 A. Flow chart of the texture analyzing and the texture 59 distributions

60 As shown in Fig. 1, the traditional texture analysis pro-  
61 cess typically comprises four key stages: First, acquisition of  
62 pole figures data for different crystallographic planes through  
63 XRD or NuD experiments, recorded using a two-dimensional  
64 position-sensitive detector. Subsequently, raw pole figures  
65 data undergo background correction and normalization to ob-  
66 tain the normalized pole density distribution. The spheri-  
67 cal harmonic expansion method is then applied to calculate  
68 the three-dimensional ODF. Finally, texture components are  
69 identified and their volume fractions quantified through ODF  
70 interpretation.



71 Fig. 1. Flow chart of the texture analyzing.

72 Due to the highly symmetric close-packed configuration of  
73 {111} crystallographic planes in FCC structured materials,  
74 which provides 12 equivalent slip systems, these materials  
75 exhibit unique advantages in ductility, toughness, and resis-  
76 tance to irradiation damage. Consequently, FCC materials  
77 are widely used in various industrial sectors, including au-  
78 tomotive, aerospace, marine, and nuclear reactor industries.  
79 The comprehensive research foundation and extensive exper-  
80 imental data available for texture studies of FCC materials  
81 make investigations into their crystallographic texture partic-  
82 ularly valuable. Given this research background, the present  
83 study focuses specifically on analyzing the texture character-  
84 istics of FCC structured materials, where the (111), (200),  
85 and (220) pole figures serve as fundamental inputs for tex-  
86 ture characterization. Six representative FCC texture com-  
87 ponents were selected for analysis: Goss[26], Brass[27–29],  
88 Cube[30], Copper[29], S[28], and R[31] orientations. Fig. 2  
89 illustrates the characteristic pole figures of these six texture  
90 components, demonstrating their distinct distribution patterns  
91 in the (111), (200), and (220) crystallographic planes. This  
92 conventional texture analysis requires approximately 5 min-  
93 utes per sample.

94 ML approaches offer significant potential for workflow op-  
95 timization. As illustrated in Fig. 1, establishing direct map-  
96 pings between pole figures and texture components could  
97 substantially enhance analysis efficiency.

100

### B. CNN texture analyzing method

#### 101 1. CNN architecture

102 CNN, a deep learning architecture specialized for process-  
103 ing grid-structured data (e.g., images, time-series signals),  
104 has demonstrated remarkable success in computer vision and  
105 materials informatics applications.

106 In this study, we employ a CNN architecture to establish an  
107 efficient mapping relationship between pole figure data and  
108 corresponding texture components with their volume frac-  
109 tions. Fig. 3 shows the architecture of the CNN model which  
110 consists of input, extraction, fully connected, and output lay-  
111 ers.

112 In our case, the input data for the input layer is

$$113 \mathbf{x}^{(0)} = \{x_1^{(0)}, x_2^{(0)}, x_3^{(0)}\} \\ = \{I_{(111)}(\chi, \phi), I_{(200)}(\chi, \phi), I_{(220)}(\chi, \phi)\}, \quad (1)$$

114  $I_{(c)}(\chi, \phi)$  is the intensity distribution on  $\chi$  (the polar angle be-  
115 tween the  $(hkl)$  crystallographic plane normal and the sample  
116 normal direction) and  $\phi$  (the azimuthal rotation angle about  
117 the sample normal axis) angle. The final output is

$$118 \mathbf{y}_i = \{V_{\text{frac}}(1), V_{\text{frac}}(2), V_{\text{frac}}(3), \\ V_{\text{frac}}(4), V_{\text{frac}}(5), V_{\text{frac}}(6)\}, \quad (2)$$

119 where  $V_{\text{frac}}(j)$  denotes the volume fractions of  $j$ -th texture  
120 components.

122 The feature extraction module comprises sequential pro-  
123 cessing through Conv\_Before, Inception\_1, Inception\_2, In-  
124 ception\_3, and Conv\_After sub-structures. Initial feature  
125 extraction occurs through Conv\_Before, followed by multi-  
126 scale feature learning via three Inception modules. The  
127 Conv\_After sub-structure finalizes the feature extraction pro-  
128 cess, preparing high-level representations for subsequent lay-  
129 ers. Architectural details are provided in Appendix Fig. 10.

130 The fully connected layer consists of six parallel hidden  
131 layers (32 neurons each) with independent parameters. These  
132 layers integrate high-dimensional features from the extraction  
133 module and perform dimensionality reduction through linear  
134 transformations, ultimately predicting the volume fractions  
135  $V_{\text{frac}}(j)$  for the six texture components via output layers.

136 In our work, the CNN model is implemented using the Py-  
137 Torch framework[32].

#### 138 2. Data set preparation

139 To facilitate ML implementation, we established a dataset  
140 comprising 137 experimentally measured pole figures: 121  
141 collected via XRD from silver-, nickel-, and copper-based al-  
142 loys, with an additional 16 aluminum alloy pole figures ac-  
143 quired through neutron diffraction experiments at the China  
144 Advanced Research Reactor (CARR).

146 All data were acquired using the equal-angle step method  
147 with  $\chi$  and  $\phi$  sampling intervals of  $5^\circ \times 5^\circ$  (Fig. 4). This an-  
148 gular resolution ensures sufficient accuracy for spherical har-

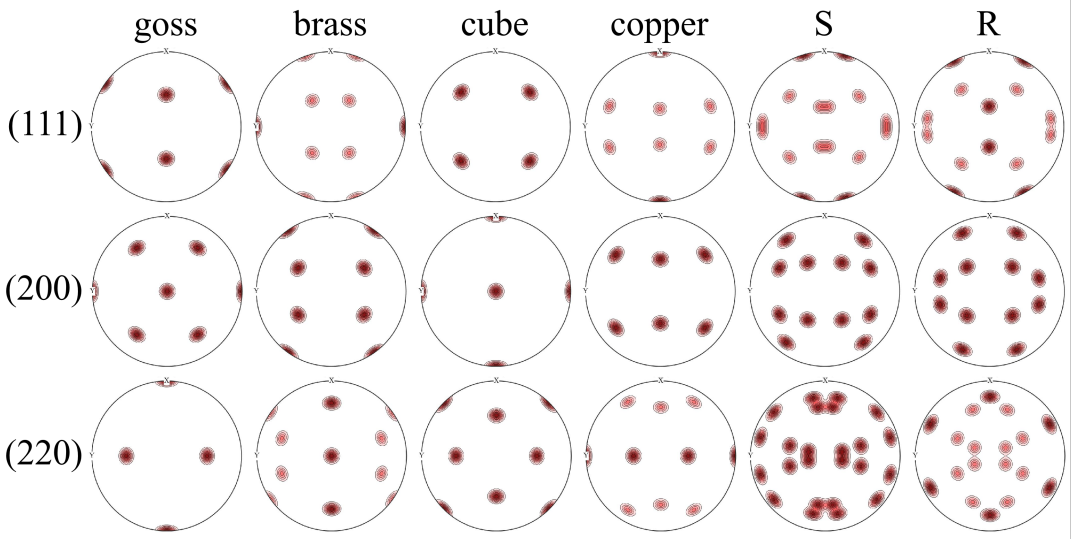


Fig. 2. Pole figures of six typical textures in the (111), (200), and (220) directions in FCC material.

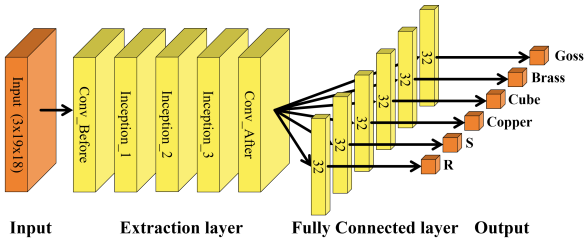


Fig. 3. Convolutional neural network structure.

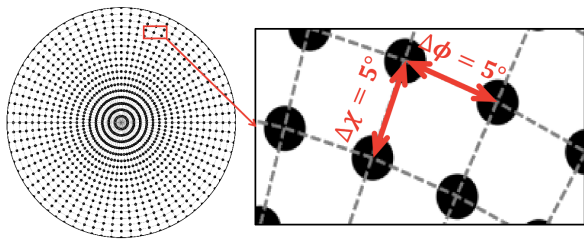


Fig. 4. Distribution of sampling points measured at equal angle intervals.

monic reconstruction while minimizing experimental data requirements, as evidenced by the resultant dataset dimensions of  $3 \times 19 \times 72$ , where the first dimension corresponds to the three crystallographic planes [(111), (200), (220)], the second dimension represents the angular sampling points along  $\chi$  ( $0^\circ$  to  $90^\circ$  in  $5^\circ$  steps), and the third dimension represents the angular sampling points along  $\phi$  ( $0^\circ$  to  $355^\circ$  in  $5^\circ$  steps). Diffraction intensities  $I_{hkl}$  were recorded at each measurement position and processed through LaboTex software (v3.0)[33] for ODF calculation. The extracted volume fractions  $V_{\text{frac}}$  of the six texture components served as labels of the dataset for subsequent ML analysis.

The total amount of raw data ( $N = 121$ ) is insufficient

to meet the training requirements of deep learning models. To address this limitation, we propose a data augmentation strategy based on the symmetry of the crystal pole figure.

The data enhancement is done by considering the symmetry properties of pole figure. Ideally, the pole figures on the (111), (220), and (222) planes exhibit mirror symmetry with the transverse direction (TD, the direction perpendicular to the main deformation direction during the processing of the material) and the rolling direction (RD, the direction along which the material is rolled during processing) as the axes of symmetry due to the geometric symmetry of the cubic sample. Thus, only 1/4 of the pole figure is useful for determining the texture in material, which means the effective data matrix will be  $3 \times 19 \times 18$  rather than the whole pole figure data, i.e.,  $3 \times 19 \times 72$ . However, due to the statistical and systematic uncertainties in the measurements, the experimental results of the pole figures do not strictly satisfy this symmetry requirement. This property suggests that we can split one pole figure to four different sub-pole figures to increase the number of training datasets in the case of weakly influence the identification of the texture type and its volume fraction. To evidence the accuracy on the identification of texture type by using 1/4 pole figure, we examined the results of texture identification by using the 1/4 pole figure shown in Fig. 5(b). Our calculations show that the predicted results are consistent with those obtained using the complete pole figures.

The following process was designed and it is shown in Fig. 5. First, three directional pole figures are divided into four parts according to the mirror symmetry axis as shown in Fig. 5(a), yielding 12 effective pole figures. Then, we randomly select a part from each directional pole figure and formatted into matrix format, reducing the  $\phi$  direction data from 72 to 18. Similar selection operations are applied to the remaining two pole figures. Finally, the three selected matrices are stacked to form a pole figure data represented in a three-dimensional matrix format (i.e.,  $3 \times 19 \times 18$ ). Through this

procedure, a dataset with  $64 \times 4 \times 4 \times 4 = 7744$  samples was formed.

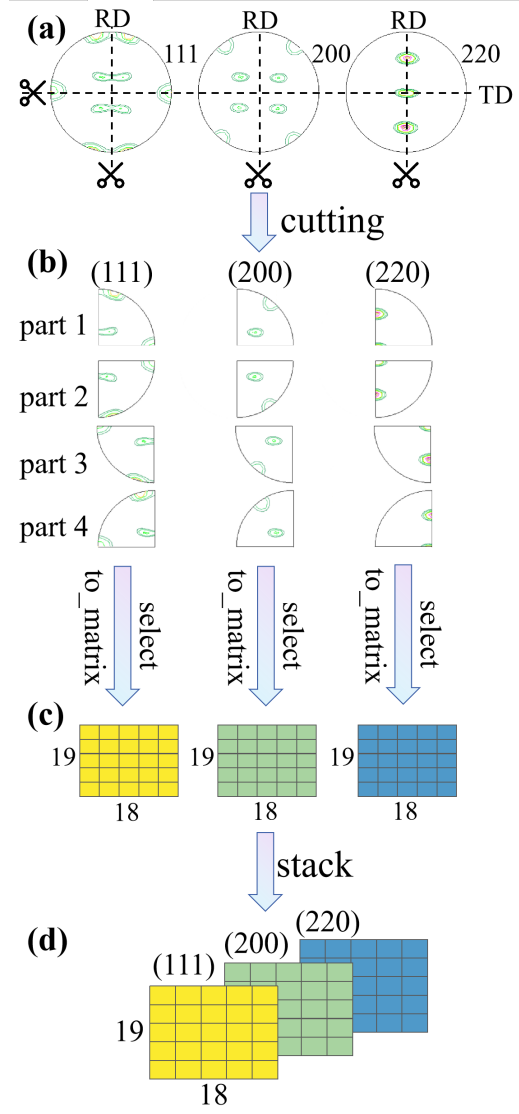


Fig. 5. Extending the number of samples in the data set by using the mirror symmetry of the pole figure.

In order to facilitate a reliable model, the data set has been divided into a training set and a validation set according to a ratio of 8:2. The model parameters are updated according to the training set during the learning process, and the validation set is employed to fine-tune the model parameters.

### 3. Data preprocessing

Before training the CNN model, the data have to be preprocessed due to the following two reasons. One is that the differences in the physical properties of X-rays and neutron rays give rise to a considerable intensity range, from  $10^2$  to  $10^5$ , as observed in the pole figure data obtained from various material tests. This large range of the intensity pose challenges

for the CNN model training. In order to ensure that the model trained using the XRD dataset can also perform effectively in the NUD prediction task, it is necessary to normalize the measurement intensity of the sample according to the following steps:

$$x(\chi, \phi) = \frac{I(\chi, \phi) - I_{\min}(\chi, \phi)}{I_{\max}(\chi, \phi) - I_{\min}(\chi, \phi)}, \quad (3)$$

where  $x$  is the reduced measured signal intensity.  $I_{\min}(\chi, \phi)$  and  $I_{\max}(\chi, \phi)$  are the minimum and maximum measured signal intensity, respectively.

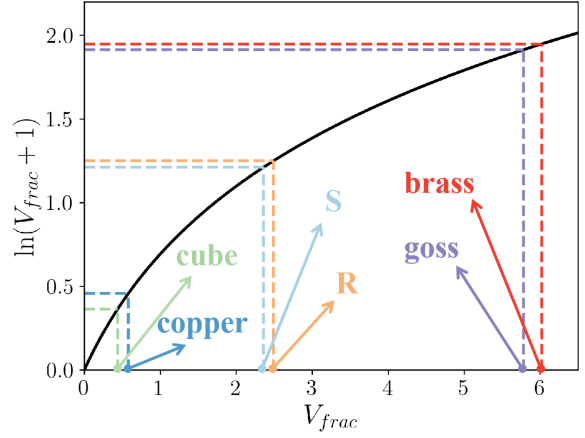


Fig. 6. The function of nonlinear mapping in the label original data space. The original data increases with a step size of 1, and the amount of data increase after nonlinear mapping becomes smaller and smaller, which can weaken the impact of large offset data.

The other is that the significant difference exists in the volume fraction  $V_{\text{frac}}$  values across different labels. As illustrated in Fig. 6, the brass component exhibits a volume fraction of 6.02%, whereas the cube component demonstrates only 0.44%. This 5.58% discrepancy between component fractions significantly impacts the model's predictive accuracy. To address this issue and improve model performance, we apply a logarithmic transformation, which can be mathematically represented as:

$$y = \ln(V_{\text{frac}} + 1). \quad (4)$$

As shown in Fig. 6, this nonlinear mapping is capable of suppressing considerable distinctions between volume fraction values while simultaneously preserving subtle differences between such values. Once the trained CNN model has been employed to calculate the normalized pole figure data, the predicted value can be utilized to ascertain the volume fraction of the texture in the material through  $V_{\text{frac}} = e^y - 1$ .

### 4. model training

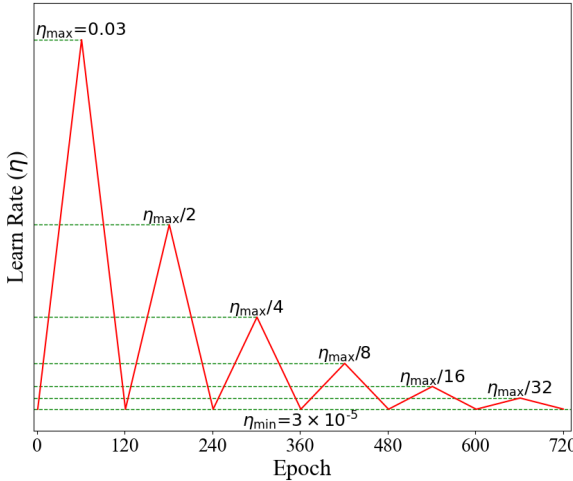
In this network architecture, the parameters are optimized using the stochastic gradient descent (SGD) algorithm, where

245 the parameter update rule is defined as:

$$246 \quad \theta_{\text{new}} = \theta_{\text{old}} - \eta \frac{\partial \mathcal{L}}{\partial \theta}, \quad (5)$$

247 where  $\eta$  is the learning rate, and  $\mathcal{L}$  is the loss function.

248 In order to ensure that the model exhibits effective predictive capabilities, it is essential to set a small learning rate. 249 However, this approach can lead to the model falling into a local minimum. Therefore, the CyclicLR learning rate scheduling strategy[34] is employed to avoid this issue and ensure the 250 model's optimal performance. The characteristic of this strategy is that the learning rate exhibits a periodic decay throughout 251 the training epochs. The learning rate varies cyclically 252 between  $3 \times 10^{-5}$  and  $3 \times 10^{-3}$ , with each 120-epoch cycle 253 reducing its maximum rate by 50% while maintaining a 254 constant minimum rate of  $3 \times 10^{-5}$ . Fig. 7 illustrates the 255 adjustment of the learning rate with the number of epochs. 256



260 Fig. 7. CyclicLR learning rate scheduling strategy.

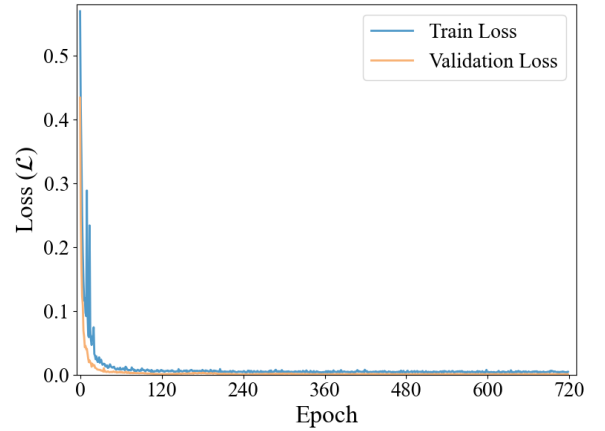
261 For the CNN model predicting volume fractions of six texture 262 components, we define the composite loss function  $\mathcal{L}$  as:

$$264 \quad \mathcal{L} = \frac{1}{N_t} \sum_{j=1}^{N_t} MSE_j, \quad (6)$$

265 Here,  $N_t$  is the number of texture components and  $MSE_j$  266 is the mean square error for  $j$ -th texture component. In this 267 work,  $N_t = 6$ . The  $MSE_j$  is given by,

$$268 \quad MSE_j = \frac{1}{N_j} \sum_{i=1}^{N_j} \left( V_{\text{frac},j}(i) - V_{\text{frac},j}^{\text{CNN}}(i) \right)^2. \quad (7)$$

269 Here,  $N_j$  is the number of samples for  $j$ -th texture component. In Fig. 8, we present the value of the loss function as a 270 function of iteration epochs, which reaches about  $5.0 \times 10^{-3}$  271 after approximately 150 epochs under the proposed optimization 272 strategy. After being tuned by the validation sets, the 273 value of the validation loss is about  $2.0 \times 10^{-3}$ , which is less 274 than that for training loss. 275



276 Fig. 8. Loss function value as a function of epoch for the training set and validation set.

## 277 5. Generalization ability under noise

278 In order to test and verify the generalization ability of the 279 CNN model, we aimed to demonstrate its capacity to predict 280 the volume fraction of textures in materials, which is mea- 281 sured by neutron diffraction. We utilized 16 sets of pole fig- 282 ure data obtained from neutron diffraction measurements to 283 validate the trained CNN model.

284 To quantify the generalization ability of the model, we an- 285 alized the differences between the prediction results of the 286 CNN model, i.e.,  $V_{\text{frac},j}^{\text{CNN}}$  and the traditional analysis re- 287 sults, i.e.,  $V_{\text{frac},j}$ . The coefficient of determination  $R^2$  is employed 288 to quantify the discrepancies between these two sets of re- 289 sults:

$$290 \quad R^2 = 1 - \frac{\sum_{i=1}^N (V_{\text{frac}}^{\text{CNN}}(i) - V_{\text{frac}}(i))^2}{\sum_{i=1}^N (\bar{V}_{\text{frac}}^{\text{CNN}} - V_{\text{frac}}(i))^2}, \quad (8)$$

291 where  $\bar{V}_{\text{frac}}^{\text{CNN}}$  represents the mean predicted value. If the pre- 292 diction can well reproduce the true data, the value of  $R^2$  is 293 closer to 1. The results of  $R^2$  calculations are displayed in 294 the yellow part of Fig. 9, where the minimum value of  $R^2$  295 is 0.98805. This shows that the model can well predict the 296 volume fraction of a certain texture from the data of neutron 297 diffraction measurement.

298 In order to ascertain the capacity of the CNN to precisely 299 predict the data at low signal-to-noise ratio, a random noise 300  $\delta I(\chi, \phi)$  obeying a uniform distribution was added to the en- 301 tire measurement region. The intensity of the noise is set 302 to 10% of the maximum value of the pole figure data, i.e., 303  $\delta I(\chi, \phi) = 10\% \times I_{\max}(\chi, \phi)$ .

304 Subsequently, the model was employed to predict texute 305 components and its fractions according to the data  $I(\chi, \phi) +$  306  $\delta I(\chi, \phi)$ . The green part of Fig. 9 shows the  $R^2$  metric pre- 307 dicted by the model after adding noise with the intensity of 308 10% of maximum strength. Comparing this to the  $R^2$  metric 309 predicted by the model with noise-free, the results with 10%

noise show a slight decrease in the accuracy of the model's predictions. However, the minimum value of the  $R^2$  value at this point is 0.94233, indicating that the model still has a high prediction accuracy. This result evidences that the prediction using CNN retains the high anti-interference ability. In cases where the intensity of the noise is greater than 10% of the maximum value of the pole figure data, the identifications become much worse.

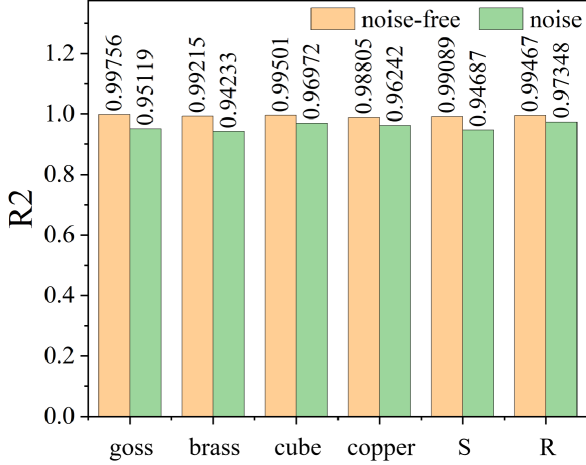


Fig. 9. The  $R^2$  metrics of the model prediction ability on the data set of neutron diffraction measurement material texture.

Finally, we also check the time consumption on the texture identification from the pole figure data. After adopting the CNN model with a trained model, the analysis time for a single sample is less than 1 second, which is 300 times faster than the traditional method.

### III. SUMMARY AND OUTLOOK

In summary, we present a CNN model that is suitable for multi-objective prediction from pole figure data obtained by XRD measurements of FCC materials. The model was trained using the SGD algorithm and subsequently tested on pole figure data obtained from neutron diffraction measurements. The analysis results demonstrate that the model retains a high degree of predictive capability on the neutron diffraction measurement data, even though the dataset originates from XRD measurements. This is attributed to latent parameters learned in the CNN model containing the correct texture component information, which makes the CNN model arrive at the correct conclusion on the texture component whatever the input data from XRD or NuD.

Furthermore, the application of the CNN model to analyze pole figure data not only enables the rapid prediction of material texture information but also exhibits considerable potential for utilization in specific scenarios. For example, the

robust data anti-interference capacity enables the delivery of precise texture information in even in a high noise conditions, which may come from the lower intensity or short measuring time. In the future, further exploration of the potential applications of the CNN model in neutron texture diffractometers, such as processing the raw data to the texture components will be conducted.

### Appendix A: Details of the extraction layers in the CNN model

Fig. 10(a)-(f) present the detailed structure of the extraction layers in the CNN model.

Panel (a) shows the CNN feature extraction layer employs Conv2dBlock (abbreviated as CB) as its fundamental building unit. Each CB sequentially integrates a convolutional layer, batch-normalization (BN) layer, and ReLU activation function in series.

The input data first enters the Conv\_Before module. As shown in Panel (b), the initial input dimensions of  $3 \times 19 \times 18$  (channels  $\times$  height  $\times$  width) are expanded to  $3 \times 21 \times 21$  through zero-padding. This is subsequently processed by three cascaded CB units: the first CB utilizes a  $1 \times 1$  convolutional kernel to expand the channel dimension to 32, the second CB employs a  $3 \times 3$  kernel for spatial feature extraction while keeping the channel count unchanged, and the third CB further extends the channels to 64 using another  $1 \times 1$  kernel. A  $3 \times 3$  max-pooling layer with stride 2 then performs spatial down-sampling, ultimately yielding feature maps of dimensions  $64 \times 10 \times 10$ .

The Inception series modules achieve multi-scale feature fusion through differentiated architectures. Specifically, the Inception\_1 module processes input features through four parallel branches (see Panel (c)): 1) a single CB with  $1 \times 1$  kernel (32 output channels), 2) a branch combining a  $1 \times 1$  CB and a  $3 \times 3$  CB (64 output channels), 3) a pathway consisting of a  $1 \times 1$  CB followed by two  $3 \times 3$  CBs (16 output channels), and 4) a branch incorporating a  $3 \times 3$  max-pooling layer with stride 1 and a  $1 \times 1$  CB (16 output channels). Channel-wise concatenation of these branches generates  $128 \times 10 \times 10$  feature maps. The Inception\_2 module (see Panel (d)) follows similar architectural principles with branch outputs of 32, 64, 16, and 16 channels (from left to right). Inception\_3 (see Panel (e)) employs six parallel branches producing 32, 32, 32, 4, 4, and 8 channels respectively, ultimately outputting high-dimensional features of size  $112 \times 10 \times 10$ .

The Conv\_After (see Panel (f)) module executes spatial compression and channel reduction on the  $112 \times 10 \times 10$  input features. This process compresses the tensor into a 512-dimensional vector through sequential operations: spatial reduction via max-pooling, channel-wise compression via large-kernel convolutions, and final flattening. These condensed features are then propagated through fully connected layers to generate quantitative predictions for six distinct texture volume fractions.

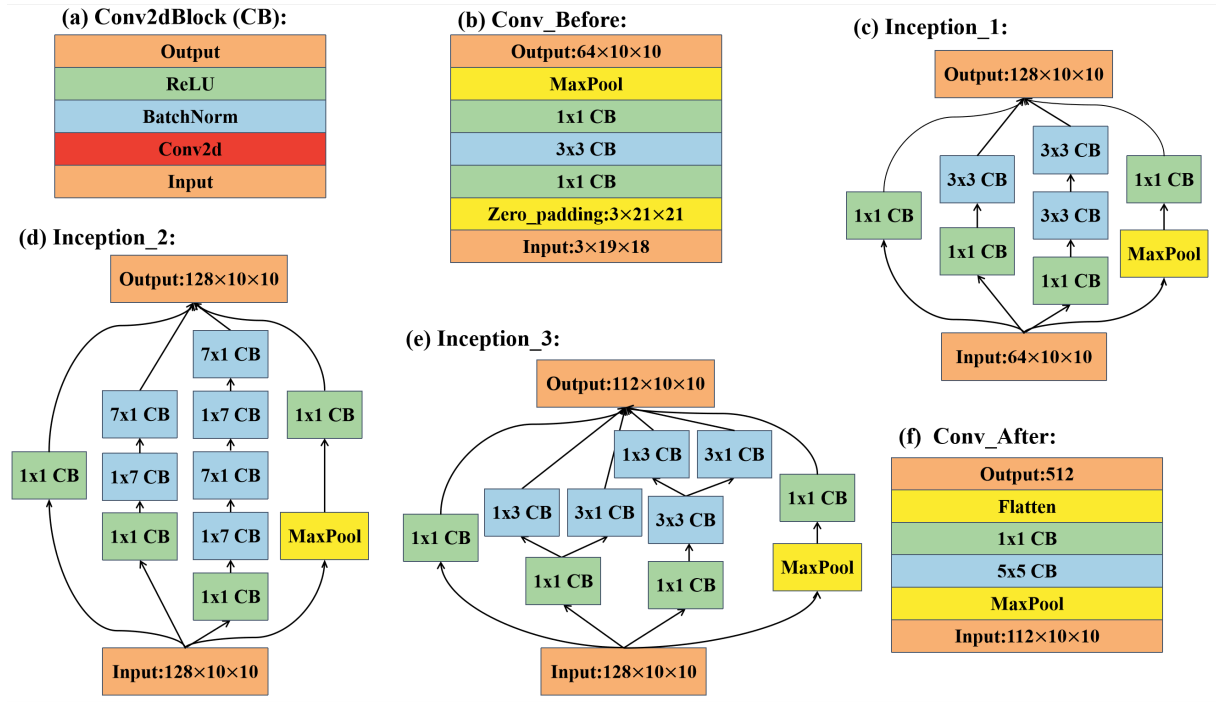


Fig. 10. The internal architecture of the extraction layers in the CNN model.

- 396 [1] Mao Weimin and Zhang Ximeng. *Quantitative Texture Anal-*  
397 *ysis of Crystalline Materials*. Metallurgical Industry Press,  
398 1993.
- 399 [2] H-R Wenk and P Van Houtte. Texture and anisotropy. *Rep.*  
400 *Prog. Phys.*, 67:1367, 2004.
- 401 [3] Olaf Engler and Valerie Randle. Introduction to texture anal-  
402 *ysis: Macrotecture, microtexture, and orientation mapping*,  
403 2000.
- 404 [4] LIU Yun-tao et al. Neutron nondestructive techniques and ap-  
405 *plications on failure analysis. Failure Analysis and Prevention*,  
406 16(1):70–75, 82, 2021.
- 407 [5] A. J. Wilkinson and T. B. Britton. Strains, planes, and ebsd in  
408 materials science. *Materials today*, 15(9):366–376, 2012.
- 409 [6] Saeed Moemeni and Kamran Dehghani. An investigation to  
410 microstructural and texture evolution during the cold rolling of  
411 al0. 3co-crfeNi high entropy alloy. *Materials Today Communi-*  
412 *cations*, 40:109654, 2024.
- 413 [7] Xiaohui Bian, Luděk Heller, Lukáš Kadeřávek, and Petr Ši-  
414 *ttnér. In-situ synchrotron x-ray diffraction texture analysis of*  
415 *tensile deformation of nanocrystalline niti wire in martensite*  
416 *state. Applied Materials Today*, 26:101378, 2022.
- 417 [8] Yu-Qing Li et al. Microstructure analysis and bulk texture  
418 *study in wide magnesium alloy sheets processed by twin-roll*  
419 *casting. Advanced Materials*, 13:1771–1780, 2021.
- 420 [9] Guijie Zhu et al. The latest progress on neutron texture diffrac-  
421 *tionometer at china advanced research reactor. Nuclear Instru-*  
422 *ments and Methods in Physics Research Section A: Accel-*  
423 *erators, Spectrometers, Detectors and Associated Equipment*,  
424 1047:167729, 2023.
- 425 [10] Guijie ZHU et al. Data analysis and processing method for  
426 two-dimensional position sensitive detector of neutron texture  
427 diffractometer at china advanced research reactor. *Atomic En-*  
428 *ergy Science and Technology*, 57(4):857, 2023.
- 429 [11] Woon Bae Park, Jiyoung Chung, Jaeyoung Jung, Keemin Sohn,  
430 Satendra Pal Singh, Myoungho Pyo, Namsoo Shin, and K-S  
431 Sohn. Classification of crystal structure using a convolutional  
432 neural network. *IUCrJ*, 4(4):486–494, 2017.
- 433 [12] Jin-Woong Lee, Woon Bae Park, Jin Hee Lee, Satendra Pal  
434 Singh, and Kee-Sun Sohn. A deep-learning technique for phase  
435 identification in multiphase inorganic compounds using syn-  
436 *thetic xrd powder patterns. Nature communications*, 11(1):86,  
437 2020.
- 438 [13] Juan Iván Gómez-Peralta, Xim Bokhimi, Nidia Guadalupe  
439 García-Peña, Patricia Quintana-Owen, and Geonel Rodríguez-  
440 Gattorno. Band-gap assessment from x-ray powder diffraction  
441 using artificial intelligence. *Journal of Applied Crystallogra-*  
442 *phy*, 55(6):1538–1548, 2022.
- 443 [14] Jin-Woong Lee, Woon Bae Park, Minseuk Kim, Satendra Pal  
444 Singh, Myoungho Pyo, and Kee-Sun Sohn. A data-driven xrd  
445 analysis protocol for phase identification and phase-fraction  
446 prediction of multiphase inorganic compounds. *Inorganic*  
447 *Chemistry Frontiers*, 8(10):2492–2504, 2021.
- 448 [15] Juan Iván Gómez-Peralta, Xim Bokhimi, and Patricia Quin-  
449 *tana. Convolutional neural networks to assist the assessment of*  
450 *lattice parameters from x-ray powder diffraction. The Journal*  
451 *of Physical Chemistry A*, 127(36):7655–7664, 2023.
- 452 [16] Kevin Kaufmann, Chaoyi Zhu, Alexander S Rosengarten,  
453 Daniel Maryanovsky, Tyler J Harrington, Eduardo Marin,  
454 and Kenneth S Vecchio. Crystal symmetry determination  
455 in electron diffraction using machine learning. *Science*,  
456 367(6477):564–568, 2020.
- 457 [17] Kevin Kaufmann, Chaoyi Zhu, Alexander S Rosengarten,

- 458 Daniel Maryanovsky, Haoren Wang, and Kenneth S Vecchio. 491  
 459 Phase mapping in ebsd using convolutional neural networks. 492  
 460 *Microscopy and Microanalysis*, 26(3):458–468, 2020.  
 461 [18] Kevin Kaufmann, Hobson Lane, Xiao Liu, and Kenneth S Vec- 493  
 462 chio. Efficient few-shot machine learning for classification of 494  
 463 ebsd patterns. *Scientific reports*, 11(1):8172, 2021.  
 464 [19] Yintao Song, Nobumichi Tamura, Chenbo Zhang, Mostafa 495  
 465 Karami, and Xian Chen. Data-driven approach for synchrotron 496  
 466 x-ray laue microdiffraction scan analysis. *Acta Crystallo-* 497  
*467 graphica Section A: Foundations and Advances*, 75(6):876– 498  
 468 888, 2019.  
 469 [20] Howard Yanxon, James Weng, Hannah Parraga, Wenqian Xu, 499  
 470 Uta Ruett, and Nicholas Schwarz. Artifact identification in x- 500  
 471 ray diffraction data using machine learning methods. *Journal 501  
 472 of Synchrotron Radiation*, 30(1):137–146, 2023.  
 473 [21] Xiaodong Zhao, YiXuan Luo, Juejing Liu, Wenjun Liu, 502  
 474 Kevin M Rosso, Xiaofeng Guo, Tong Geng, Ang Li, and Xin 503  
 475 Zhang. Machine learning automated analysis of enormous syn- 504  
 476 chrotron x-ray diffraction datasets. *The Journal of Physical 505  
 477 Chemistry C*, 127(30):14830–14838, 2023.  
 478 [22] Yiqing Hao et al. Machine-learning-assisted automation of 506  
 479 single-crystal neutron diffraction. *Journal of Applied Crystal- 507  
 480 lography*, 56(2):519–525, 2023.  
 481 [23] Mathieu Doucet et al. Machine learning for neutron reflectom- 508  
 482 etry data analysis of two-layer thin films. *Machine Learning:* 509  
*483 Science and Technology*, 2(3):035001, 2021.  
 484 [24] Daniil Mironov et al. Towards automated analysis for neu- 510  
 485 tron reflectivity. *Machine Learning: Science and Technology*, 511  
 486 2(3):035006, 2021.  
 487 [25] Davide Micieli et al. Accelerating neutron tomography exper- 512  
 488 iments through artificial neural network based reconstruction. 513  
 489 *Scientific Reports*, 9(1):2450, 2019.  
 490 [26] Fei Liu, Zhiyi Liu, and Guangyu He. Making al-cu-mg alloy 514  
 491 tough by goss-oriented grain refinement. *Journal of Alloys and 515  
 492 Compounds*, 904:164095, 2022.  
 493 [27] Qi Zhao, Zhiyi Liu, Shasha Li, Tiantian Huang, Peng Xia, 516  
 494 and Luqing Lu. Evolution of the brass texture in an al-cu-mg 517  
 495 alloy during hot rolling. *Journal of Alloys and Compounds*, 518  
 496 691:786–799, 2017.  
 497 [28] Swati Mahato, Nilesh P Gurao, and Krishanu Biswas. The role 519  
 498 of temperature and strain on the deformation behaviour and mi- 520  
 499 crostructural evolution of fcc (crfeni) 99si1 medium-entropy 521  
 500 alloy. *Materials Science and Engineering: A*, 922:147600, 501  
 502 2025.  
 503 [29] Krzysztof Wierzbowski, Marcin Wroński, and Torben Lef- 504  
 505 ffers. Fcc rolling textures reviewed in the light of quantita- 506  
 507 tive comparisons between simulated and experimental tex- 508  
 509 tures. *Critical reviews in solid state and materials sciences*, 509  
 510 39(6):391–422, 2014.  
 511 [30] Supriyo Chakraborty, Chaitali S Patil, Yunzhi Wang, and 512  
 512 Stephen R Niezgoda. Investigating the origin of cube texture 513  
 513 during static recrystallization of fcc metals: a full field crystal 514  
 514 plasticity-phase field study. *arXiv preprint arXiv:2006.06475*, 515  
 515 2020.  
 516 [31] Bevis Hutchinson. The cube texture revisited. In *Materials Sci- 517  
 517 ence Forum*, volume 702, pages 3–10. Trans Tech Publ, 2012.  
 518 [32] Adam Paszke et al. Automatic differentiation in pytorch. *NIPS*, 519  
 519 2017.  
 520 [33] K Pawlik and P Ozga. Labotex: the texture analysis soft- 521  
 521 ware. *Göttinger Arbeiten zur Geologie und Paläontologie*, SB4,  
 522 pages 146–147, 1999.  
 523 [34] Leslie N Smith. Cyclical learning rates for training neural net- 524  
 524 works. In *2017 IEEE winter conference on applications of 525  
 525 computer vision (WACV)*, pages 464–472. IEEE, 2017.